Atmosphere **2014**, *5*, 699-719; doi:10.3390/atmos5040699

OPEN ACCESS

atmosphere

ISSN 2073-4433

www.mdpi.com/journal/atmosphere

Article

Aerosol Optical Properties of a Haze Episode in Wuhan Based on Ground-Based and Satellite Observations

Miao Zhang [1,2], Yingying Ma [1,2,*], Wei Gong [1,2] and Zhongmin Zhu [3]

[1] State Key Laboratory of Information Engineering in Surveying, Mapping and Remote Sensing, Wuhan University, Wuhan 430079, China; E-Mail: zm_liesmars@whu.edu.cn

[2] International Research Center of Satellite Remote Sensing and Atmospheric Monitoring, Wuhan University, Wuhan 430079, China; E-Mail: weigong@whu.edu.cn

[3] Huazhong University of Science and Technology Wuchang Branch, Wuhan 430064, China; E-Mail: zhongmin.zhu@gmail.com

* Author to whom correspondence should be addressed; E-Mail: yym863@gmail.com; Tel.: +86-1592-7259-579.

External Editor: Huiting Mao

Received: 7 May 2014; in revised form: 9 September 2014 / Accepted: 24 September 2014 / Published: 15 October 2014

Abstract: A severe haze episode that occurred in Wuhan, central China, from 6–14 June 2012 was investigated using ground-based and satellite-derived observations, from which the optical properties and vertical distribution of the aerosols were obtained. The mass concentrations of $PM_{2.5}$ and black carbon (BC) were 9.9 (332.79 *versus* 33.66 $\mu g \cdot m^{-3}$) and 3.2 times (9.67 *versus* 2.99 $\mu g \cdot m^{-3}$) greater, respectively, on haze days than during normal weather. The large aerosol loading contributed to the high values of the scattering (2.32 km^{-1}) and absorption coefficients (0.086 km^{-1}). Particle size became larger, consistent with the reduced scattering Ångström exponent. The high asymmetry parameter (0.65) and single scattering albedo (SSA) (0.97) observed in the haze, which coincided with the relatively low backscatter ratio (0.11) and up-scatter fraction (0.23), were related to the increased particle size, and could have had a heating effect on the atmosphere. Aerosols accumulated primarily below 3 km and according to CALIPSO, were regular in their shapes. At the surface, the aerosol extinction coefficient detected by satellite remained at ~1 km^{-1}, very close to the ground-based observations. Aerosol optical properties measured at this downtown site could help further the understanding of the effects of aerosols on the air quality, city environment, and radiation balance.

Keywords: haze; aerosol; optical properties; nephelometer; aethalometer; CALIPSO

1. Introduction

The Intergovernmental Panel on Climate Change has reported that atmospheric aerosol radiative forcing could have significant effect on climate change [1]. Aerosols affect Earth's radiation balance directly by scattering and absorbing solar shortwave and longwave radiation. They also act as condensation nuclei for clouds, thereby changing the cloud's microphysical properties and life cycles and thus, indirectly affect the climatic system [2]. China's rapid economic growth, urbanization, population expansion, and increased industrial activity have led to increasing amounts of particles being discharged into the environment, resulting in frequent air pollution events [3]. The World Health Organization has indicated that aerosols (especially fine particles) could produce adverse effects on human health [4] and therefore, serious regional haze incidents have been investigated in many parts of China, including the Pearl River Delta, Yangtze River Delta, and Beijing–Tianjin–Hebei region (BTH) [5].

Haze episodes have attracted considerable attention from researchers and many experiments have been conducted to study haze all over the world. Since 1990 in BTH, the number of days with haze has increased gradually and the visibility has decreased continuously between 1980 and 2008 [6]. Many air pollutants accumulate during haze episodes, leading to an increase of the aerosol optical depth (AOD) [7]. In northern China, high aerosol loading at the surface has led to a decreasing trend in solar radiation at a rate of 30–40 $W \cdot m^{-2}$ per day [8]. See *et al.* reported that the concentration of $PM_{2.5}$ doubles on haze days [9]. Sun *et al.* also discovered that on hazy or foggy days, the concentration of water-soluble ions is more than 10 times that during normal weather [10]. In Guangzhou, fine particles were found to play a dominant role during haze and they exhibited a double peak in the particle size distribution [11]. A long-term study of haze in Nanjing has indicated a rapid increase in the concentration of aerosols with diameters of 0.6–1.4 μm, which has led to a significant growth in the scattering coefficient [12]. In hazy regions, increased amounts of absorbing aerosols, (e.g., dust and black carbon (BC)) can induce anomalous water cycle feedback, which can affect the general circulation and alter the dynamical state of the entire monsoon system [13–15]. Furthermore, atmospheric radiation mechanisms and agricultural activities could also be affected by haze on regional and global scales. Soot particles play the role of an absorbent, which heats the atmosphere and cools the Earth's surface [16–20]. Experts have estimated that regional haze events in China could lead to a 5%–30% decrease in crop yields [21].

Generally, haze episodes are air pollutant layers consisting of anthropogenic sulfate, nitrate, organics, BC, soot, and fly ash, as well as natural aerosols such as sea salt and mineral dust. Research has indicated that common hazes are caused mainly by anthropogenic emission sources, such as communications and transportation industries, industrial production, and cooking [22]. The study by Zhang *et al.* proved that haze pollutants comprise particles both from local emission sources and from long distance transport [23]. Owing to weather patterns, particles can be transferred on the continental scale, which greatly affects the air quality of locations in downwind directions [24,25]. Furthermore, Li *et al.* and Duan *et al.* studied the phase and mixture status of aerosols and discovered that hazes in

the North China Plain (NCP) during June are caused primarily by particles generated from the combustion of agricultural biomass [26,27].

Most haze studies in China have been undertaken in eastern [12], southern coastal [11], and northern areas [3,10,16], which have traditionally been the most polluted. However, central China has also experienced a series of significant haze episodes. To further the understanding of the causes and environmental effects of haze episodes in central China, we conducted a comprehensive study in Wuhan during 6–14 June 2012. The Hybrid Single-Particle Lagrangian Integrated Trajectory (HYSPLIT) model and Moderate-resolution Imaging Spectroradiometer (MODIS) active fire products were used to trace the source of the haze. In addition, the aerosol optical properties in Wuhan were measured using ground-based equipment that included an integrated nephelometer, aethalometer, meteorological station, and particle detector. The vertical distribution of the aerosols was obtained from the Cloud-Aerosol Lidar and Infrared Pathfinder Satellite Observation (CALIPSO) satellite.

2. Equipment and Method

2.1. Ground-Based Instruments

A nephelometer can measure the scattering and backscattering coefficients of atmospheric aerosols. An integrated nephelometer (model 3563; TSI Inc., MN, USA) with triple wavelengths (450, 550, and 700 nm) was used in the present study. Automatic zero calibration was performed daily, standard CO_2 was used as the span gas during the half-yearly span checking [28], and the equipment was calibrated a week prior to the experiment. When in operation, a built-in turbo-blower transfers air samples into the measuring chamber through a large feeding port at a flow rate of 30 $L \cdot min^{-1}$. The average sampling time was set to 1 min. The sensitivity of the equipment when measuring the light scattering coefficient was 2.0×10^{-7} m^{-1} and the response time was less than 10 s. The observation angle was 7°–170° with the truncation error limited to 10% or less [29].

The truncation error increases when large aerosol particles (such as dust) exist. Its correction is usually achieved based on the Mie theory and statistical features [30]. In the present study, the correction was performed based on the latter. For the wavelengths 450, 550, and 700 nm, the detection limits of the total scattering coefficient are 0.44, 0.17, and 0.26 Mm^{-1}, respectively, and those for the backscattering coefficient are 0.29, 0.11, and 0.21 Mm^{-1}, respectively [31]. Values lower than the detection limits were excluded from the analysis. Observation errors were derived mainly from truncation errors, non-Lambert characteristics of the light source, non-idealized wavelengths, and uncertainties in calibration. These factors contributed to approximately 7% of the determined data error [28,30].

An aethalometer (AE-31; Magee Scientific Corp., CA, USA) was employed to obtain the mass concentration of BC. It uses seven wavelengths: 370, 470, 520, 590, 660, 880, and 950 nm, and the aerosol absorption coefficient is retrieved based on the BC mass concentration. The aethalometer measures the real-time light attenuation caused by particles clustered on the quartz filtration membrane. It is assumed that the light attenuation is caused by BC absorption. Therefore, the BC mass concentration can be calculated continuously based on changes in the light attenuation [31]. On a unit

area of the filtration membrane, light attenuation exhibits a linear relationship with the BC mass concentration as follows:

$$\Delta ATN_\lambda = \ln\left(\frac{I_0}{I}\right) = \delta_\lambda \cdot BC \quad (1)$$

Here, ΔATN_λ is the light attenuation at wavelength λ within the sampling period; I_0 and I are the light intensities that pass through the filtration membrane before and after sampling, respectively; and δ_λ is the attenuation coefficient at wavelength λ (units = $m^2 \cdot g^{-1}$). For this study, the aethalometer was installed on the top of the lab building in a position free of any obstruction. The flow rate was 5 $L \cdot min^{-1}$ with a 2-min sampling time. The instrument inlet was connected through a 2.5-m-long black tube, the interior of which was coated with Teflon; hence, sample loss (particles attaching to the tube wall) could be neglected. A 2.5-μm sampling head was installed in the experiment. Quality assurance measures included checking the stability of the light source, periodic calibration of flow rate (half-yearly), and control over the aerosol load on the filtration membrane (proportion of light attenuation was controlled at 75% and below).

A PH-1 automatic weather station was also set up to measure routine meteorological variables that comprised temperature, relative humidity, pressure, and wind speed and direction [32]. Mass concentration of $PM_{2.5}$ was measured using the GRIMM 180 (GRIMM Aerosol Technik GmbH & Co., Ainring, Germany) particle detector.

2.2. Satellite Remote Sensing Observations

To trace the source of haze in Wuhan, the backward trajectory of the air mass was analyzed using the HYSPLIT model developed by the National Oceanic and Atmospheric Administration (http://ready.arl.noaa.gov/ HYSPLIT.php). Wuhan was defined as the terminal point and the backward trajectories of the air mass at 500 m above sea level were calculated for the period 7–11 June 2012. The MODIS active fire detection technique, based on Advanced Spaceborne Thermal Emission and Reflection Radiometer imagery, has become relatively well developed [33–38], and MODIS fire products were adopted in this study to both help establish the fires distribution diagram and investigate the source of the haze.

The CALIPSO satellite was launched in April 2006 and it belongs to the A-train satellite constellation. The Cloud-Aerosol Lidar with Orthogonal Polarization (CALIOP) system, loaded on CALIPSO, emits 532 and 1064 nm lasers vertically downward, receiving backscattered energy from both the atmosphere and the surface [39]. The CALIPSO satellite provides information on the vertical distribution and optical properties of aerosols and clouds at both regional and global scales, which is useful for improving the understanding of the effects of aerosols and clouds on radiation [39–41]. CALIPSO has been widely applied in research on dust and haze [42,43], e.g., the radiation heating effect of dust plumes in Tibet, caused by long-distance transport of dust arising from sandstorms in the Taklimakan Desert, has been investigated [44]. Furthermore, the optical and microphysical properties and vertical distribution of aerosols in Shanghai have been measured by CALIPSO on haze days [45]. Therefore, to further the understanding of the vertical structure and characteristics of aerosols in Wuhan, CALIPSO was employed in this study.

3. Results and Discussion

3.1. Identification and Source of Haze

The experiment was performed at the State Key Laboratory of Information Engineering in Surveying, Mapping, and Remote Sensing site, Wuhan University, where the ground-based equipment mentioned above was installed. The location of the study area is shown in Figure 1. Wuhan is a highly industrialized inland mega city in central China. It is the capital of Hubei Province and is located at the junction of the Yangtze and Han rivers. This area experiences a typical northern subtropical humid monsoon climate with high annual average temperature (15.7–17.5 °C) and precipitation (1050–2000 mm) [32]. At present, there is no globally consistent definition of haze. The Chinese Meteorological Administration (CMA) defines haze as conditions with visibility <10 km, whereas some studies have adopted a visibility criterion of <5 km [46,47]. For all previous studies, visibility has been adopted as the basic index; however, because both haze and fog result in reduced visibility, on 1 June 2010, the CMA issued a standard for haze observation and forecasting in China. This standard defines haze as visibility <10 km when relative humidity (RH) is <95%. However, this study has considered haze as conditions where the horizontal visibility is <5 km and RH is <80%, which is consistent with the study of Zhang *et al.* [23].

Figure 1. Location of study area: (**a**) location of Hubei Province, China and (**b**) location of Wuhan in Hubei Province (solid black line represents the CALIPSO track passing over Wuhan).

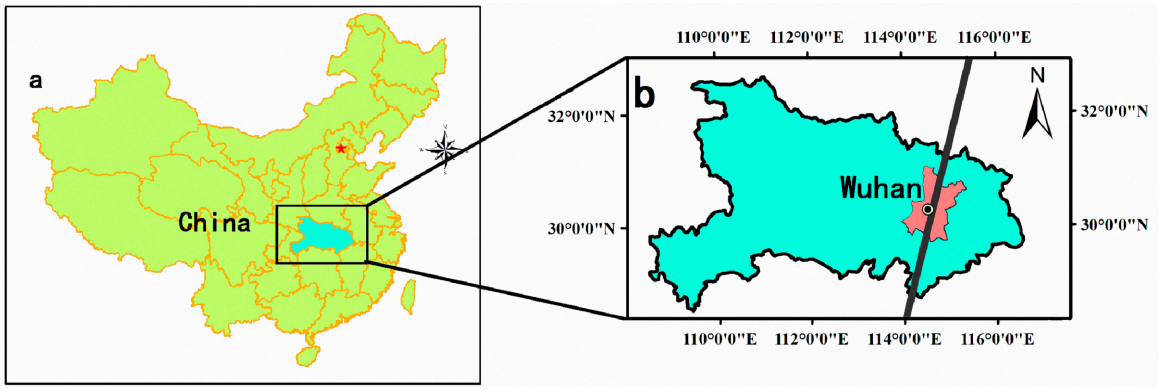

(**a**) (**b**)

The MODIS active fires distribution during 8–11 June 2012 is shown in Figure 2a. Fires were very dense in northern Anhui Province, northern Jiangsu Province, and Shandong Province. Because it was the crop-harvesting season, large amounts of biomass (such as straw) were combusted and many aerosol pollutants emitted into the atmosphere. It has been discovered that the harvest season in northern Anhui Province is in June (summer) and considerable biomass is burned during this time; thus, the fire density is much greater in June than in other months [48].

A five-day back-trajectory of air mass at 500 m above sea level was performed to establish the source of the haze and the result is shown in Figure 2b. It is clear that air masses traveled from the East China Sea and across the Yellow Sea and Shandong and Anhui provinces before finally arriving in Wuhan on the morning of 11 June, countering a few pollution sources along their path. It is also apparent from Figure 3a that a northeasterly wind was prevailing in Wuhan on the morning of 11 June.

Based on the fires distribution information, it can be speculated that the serious haze event that began in Wuhan on the morning of 11 June was caused by air mass transport bringing large amounts of pollutants, mainly from biomass combustion in northern Anhui Province near Wuhan.

Figure 2. (**a**) Active fire data during 8–11 June 2012, in Hubei Province and surrounding provinces from MODIS global fire area products (MCD14ML) (Fire pixels are shown as orange dots); (**b**) HYSPLIT backward trajectories for haze episode in Wuhan during 7–11 June 2012 (Red denotes backward trajectories arriving at heights 500 m above ground level).

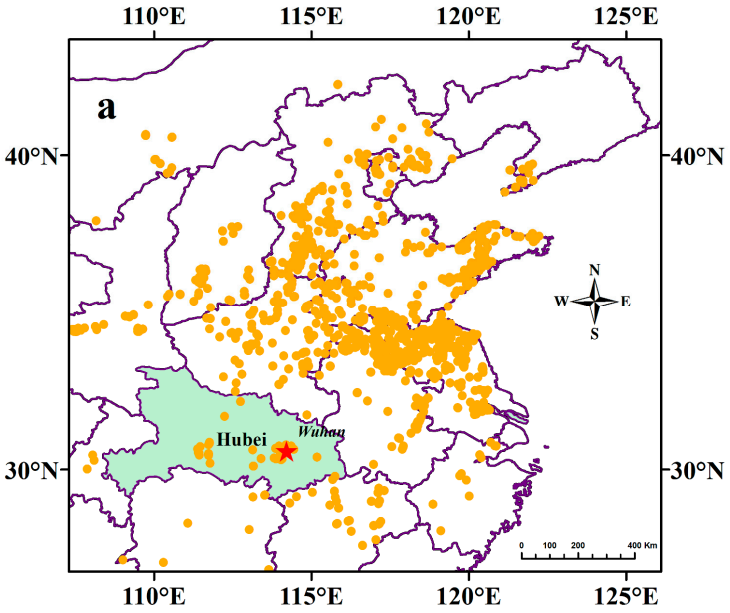

(**a**)

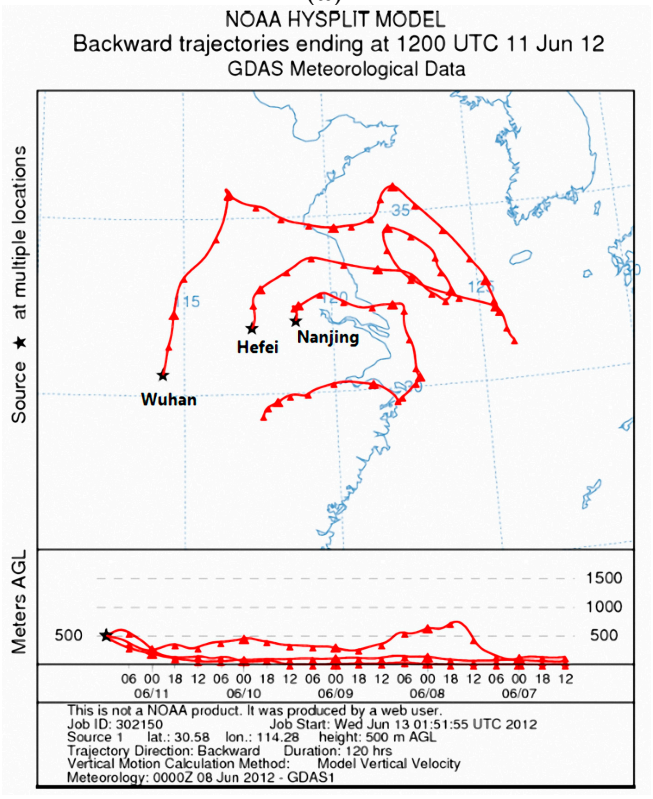

(**b**)

Figure 3. Time series variations of meteorological parameters and pollutant mass concentrations (BC and $PM_{2.5}$) at LIESMARS site during 6–14 June 2012. (**a**) Wind direction (degrees) and wind speed ($m \cdot s^{-1}$); (**b**) Temperature (°C) and atmospheric pressure (hPa); (**c**) Visibility (km) and relative humidity (%), and (**d**) BC and $PM_{2.5}$ mass concentrations and ratio between BC and $PM_{2.5}$.

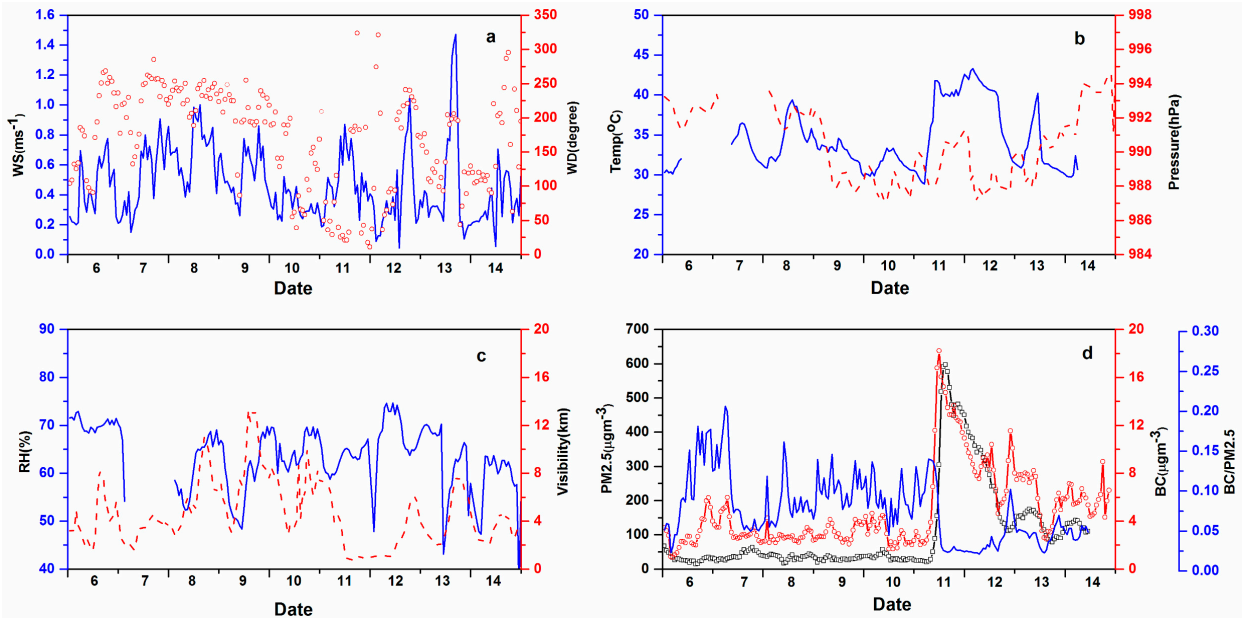

3.2. Meteorological Conditions and Pollutant Concentrations

As shown in Figure 3a, the wind direction was northeasterly on the afternoon of 10 June, and it persisted until the evening of 12 June. As explained in Section 3.1, the northeasterly winds aided the transport of particles across Wuhan, which was within a relatively weak low-pressure system during 9–13 June, as shown in Figure 3b. These meteorological conditions were not conducive to the dissipation of atmospheric particles and thus, led to the accumulation of pollutants in localized areas when the particulate matter arrived over Wuhan. Before the haze event, surface temperature exhibited a characteristic diurnal variation; however, during the haze event, surface temperature increased dramatically between noon on 11 June and the evening of 13 June. During this period, there was no visible diurnal change in temperature, which remained at 35–40 °C. Wang and Xia have both reported that particles have a heating effect on the environment during haze episodes [16,18]. Due to biomass combustion, the number of soot particles increases significantly, which can be revealed through the enhanced BC mass concentration, as discussed in the next paragraph. Soot pollutants can heat the atmosphere and affect the radiative effect of aerosols on the atmosphere [19,20]. It can be seen from Figure 3c that there was also significant diurnal change in RH before the haze event, but that RH remained at the high level of 60%–70% during the haze event of 11–13 June. Visibility also decreased to about 1 km by noon on 11 June and these conditions lasted until noon on 12 June. The minimum visibility reported was 0.72 km.

Figure 3d shows that the mass concentrations of $PM_{2.5}$ and BC increased sharply in the morning of 11 June and reached maximum values of 597 and 18 $\mu g \cdot m^{-3}$, respectively, at noon on the same day. During the haze period, the mean $PM_{2.5}$ and BC mass concentrations were approximately 9.9 (332.79

versus 33.66 μg·m^{-3}) and 3.2 times (9.67 *versus* 2.99 μg·m^{-3}) greater, respectively, than during the non-haze period. Because of the large quantities of highly concentrated particles that were transported to the local area within a short time, the mass concentration of particles remained at a high level during 11–13 June. Before the haze period, BC/$PM_{2.5}$ was maintained at ~0.13, but it decreased rapidly to 0.025 once the haze developed and remained <0.1 (~0.06) throughout the days of haze. This indicates that the quantities of both non-BC and BC aerosols increased significantly. However, the proportion of non-BC aerosols increased more rapidly than that of BC aerosols. The statistical information regarding the meteorological parameters and particle concentrations measured during the experiment is summarized in Table 1.

Table 1. Meteorological information obtained during the study.

Date	WS (m·s^{-1})	WD (Degrees)	Temp (°C)	Pressure (hPa)	RH (%)	Visibility (km)
6 June 2012	0.41 (0.21, 0.68)	181.95 (95.00, 256.13)	30.27 (29.84, 30.64)	992.44 (991.48, 992.99)	70.13 (68.62, 71.59)	3.62 (1.81, 6.75)
7 June 2012	0.57 (0.22, 0.78)	226.48 (150.27, 258.59)	30.08 (29.79, 31.40)	992.42 (991.61, 993.24)	60.55 (59.36, 68.21)	3.46 (1.78, 4.30)
8 June 2012	0.69 (0.42, 0.90)	234.50 (203.62, 250.28)	32.43 (30.89, 35.96)	992.12 (991.28, 992.84)	64.15 (52.87, 67.59)	5.41 (3.08, 9.72)
9 June 2012	0.50 (0.34, 0.72)	214.82 (152.79, 239.41)	34.65 (32.79, 38.56)	988.31 (987.82, 991.85)	60.67 (49.60, 67.68)	7.55 (3.50, 12.93)
10 June 2012	0.31 (0.24, 0.43)	133.40 (56.58, 190.36)	31.96 (29.86, 33.53)	987.88 (987.20, 989.00)	64.72 (60.72, 69.53)	6.38 (3.63, 8.55)
11 June 2012	0.47 (0.21, 0.74)	42.65 (19.33, 186.79)	31.20 (29.17, 33.00)	989.95 (988.04, 990.79)	63.08 (59.79, 65.45)	1.09 (0.77, 6.91)
12 June 2012	0.32 (0.11, 0.73)	185.02 (47.64, 240.46)	40.64 (36.42, 42.65)	987.91 (987.44, 989.73)	66.93 (51.15, 73.95)	1.72 (1.04, 5.47)
13 June 2012	0.32 (0.18, 1.08)	124.87 (79.89, 198.18)	34.54 (31.13, 41.12)	990.17 (988.27, 990.98)	65.08 (45.20, 69.89)	3.62 (2.09, 7.45)
14 June 2012	0.26 (0.21, 0.55)	128.10 (92.22, 242.92)	30.90 (29.78, 36.92)	993.50 (991.20, 994.38)	59.89 (47.53, 63.07)	3.29 (2.09, 4.34)

Median values are stated on the top line and the 10th and 90th percentiles are stated underneath within the parentheses.

3.3. Aerosol Optical Properties

3.3.1. Aerosol Scattering Properties

(1) Aerosol Scattering Coefficient

The scattering coefficient of aerosols is an important value among the aerosol optical properties, because it reflects the scattering ability of the aerosols. The scattering coefficient variation at the wavelength of 550 nm (σ_s_550) is shown in Figure 4a. It increased sharply during the haze period and reached its maximum value of 4.49 km^{-1} during the afternoon of 11 June, which was the day with the worst conditions. During the haze, the mean value (2.32 km^{-1}) was approximately 5.3 times that of normal weather (0.44 km^{-1}). This result indicated that the haze episode was severe and that it could

have had adverse effects on human health. Zhang *et al.* found that the mean value of σ_s_550 on the eastern coast of China (ECH) under haze conditions was 1.050 km^{-1}, and that the maximum value for ECH was 1.310 km^{-1} [23]. In a winter regional haze event in the NCP, the mean value of the scattering coefficient was determined as 0.58 km^{-1}, which is 8.1 times higher than on non-haze days [3]. At Wuqing, Ma *et al.* found a mean scattering coefficient of 0.74 km^{-1} during a pollution episode in spring and 0.87 km^{-1} in summer [49]. Both values are lower than that determined in Wuhan, indicating the severity of the Wuhan event. The rapid increase of the aerosol scattering coefficient was attributed mostly to the large local aerosol loading within the regional transport.

Figure 4. Time series variations of aerosol optical properties during haze at LIESMARS site during 6–14 June 2012. (**a**) Aerosol total scattering coefficient σ_s_550 (km^{-1}) at wavelength of 550 nm and absorption coefficient σ_{ab}_532 (km^{-1}) at 532 nm; (**b**) Scattering Ångström exponents α_s and backscatter ratio b_550 at wavelength of 550 nm; (**c**) Up-scatter fraction β_550 and asymmetry parameter g_550 at wavelength of 550 nm; and (**d**) SSA ω_0 at wavelength of 532 nm.

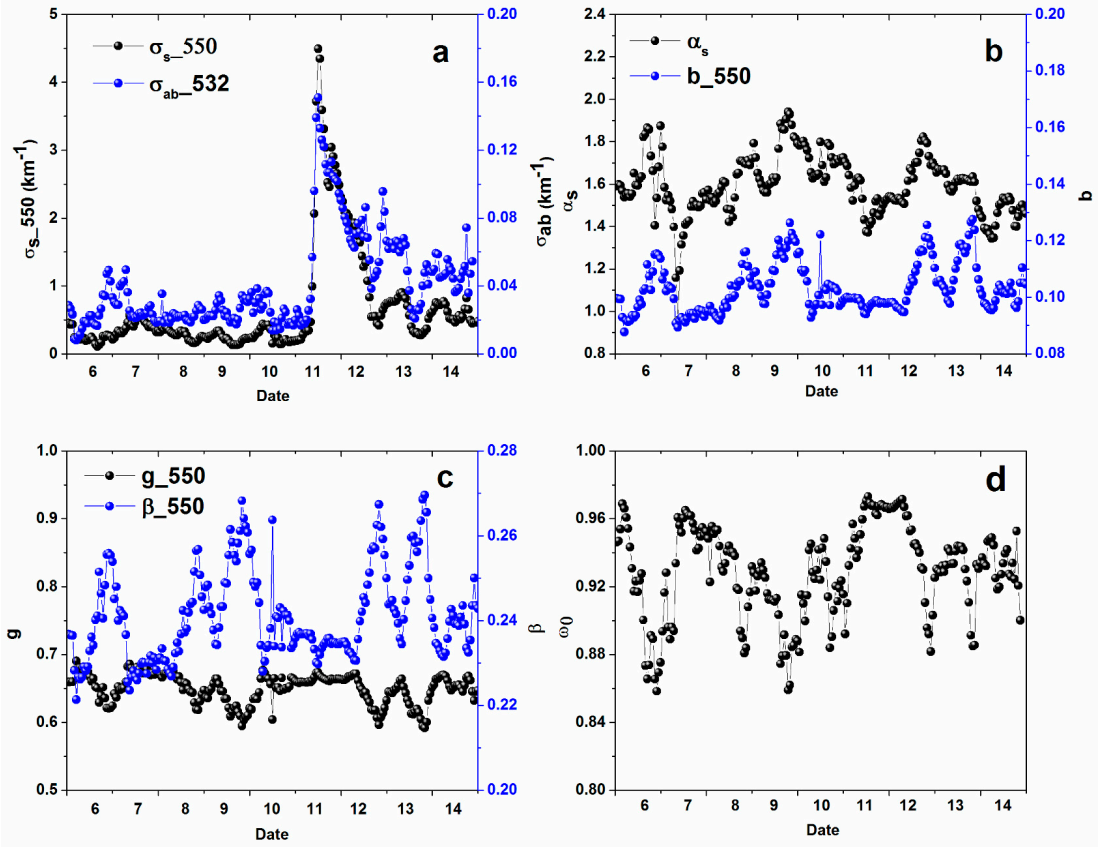

(2) Aerosol Scattering Ångström Exponent

The aerosol scattering Ångström exponent (α_s) reveals aerosol size information according to the Mie theory. It can show that a decreasing trend with increasing aerosol size [23] is related to the spectral dependence of the aerosol scattering coefficient, and can be measured using a multi-wavelength nephelometer. The value of α_s is determined by the aerosol size distribution and refractive index, and

exhibits little relationship with aerosol concentration. Generally, it can be described using an empirical equation in the range of the visible spectrum:

$$\sigma_s(\lambda) = \beta_s \cdot \lambda^{-\alpha_s} \quad (2)$$

Here, $\sigma_s(\lambda)$ is the aerosol scattering coefficient at wavelength λ, β_s is the conversion constant, and α_s is the dimensionless scattering Ångström exponent. In order to cover a wide wavelength range, α_s was calculated for wavelengths of 450 and 700 nm using the following formula:

$$\alpha_s = -\ln\left[\frac{\sigma_s(\lambda_1)}{\sigma_s(\lambda_2)}\right] \cdot \left[\ln\left(\frac{\lambda_1}{\lambda_2}\right)\right]^{-1} \quad (3)$$

Figure 4b shows the variation of α_s during this study. As shown, α_s decreased rapidly from 1.7 in the morning to around 1.3 at noon on 11 June, and remained consistently at about 1.4 until noon on June 12. This result indicates that particle size increased during the haze period. In the study by Zhang *et al.*, the mean value of α_s during the haze episode was 1.33, indicating that larger particles dominated in the haze [23]. In the current study in Wuhan, the α_s value of 1.4 indicates the growth trend of particle size, but that the particle size was not large and that the majority of aerosols were still fine particles. Zhang *et al.* reported that haze episodes caused by plumes transported over long distances often have higher values of α_s than haze caused by local emissions, and that long-distance transport appears to assist the formation of haze episodes [23]. In the present study, the relatively high value of α_s is consistent with the conclusions of Zhang *et al.*; however, the results of Tan *et al.* from a study in Guangzhou also demonstrated that fine particles can play a dominant role in causing haze [11].

Particles emitted from biomass combustion can increase in size during long-distance transport, leading to a decreasing trend of α_s [50], because particles can experience processes of solidification and condensation during transportation [51]. In such cases, aerosols also undergo an aging process over time, which also acts to increase particle size. Previous studies by Eck *et al.* [52,53] and O'Neill *et al.* [54] have indicated that α_s can be reduced by >50% during the aging process of particles. Moreover, during long-distance transport, water-soluble secondary aerosols could be formed in haze. Owing to the comparatively higher RH during the haze period, such hydrophilic aerosols would have easier access to water, which would also result in increasing particle sizes [55].

(3) Aerosol Asymmetry Parameter and Backscatter Ratio

The aerosol asymmetry parameter (g) reflects the forward scattering capability of particles and is typically dependent on the scattering phase function. The backscatter ratio (b) is defined as the ratio of the coefficient of aerosol backscattering to the scattering coefficient. When light reaches the aerosol surface, it is partly scattered back into space, resulting in a cooling effect on the atmosphere. This scattered part is known as the up-scatter fraction (β), which can be considered as the ratio of light scattered back into space to the total scattered light [23]. Here, b can be measured using a nephelometer. The aerosol asymmetry parameter and up-scatter fraction can both be retrieved based on the backscatter ratio. These three physical quantities reflect the specific scattering effects of aerosols within the total scattering. Thus, investigations into g, b, and β can help improve the understanding of aerosol optical properties during haze periods.

Figure 4b shows b_550 obtained by nephelometer at the green wavelength (550 nm) during the experimental period. Before the haze occurred, b_550 was ~0.12 on 10 June; it then decreased to 0.10 on 11 June, before recovering to ~0.12 following the disappearance of the haze. Zhang *et al.* also reported a mean value of b of 0.10 for a haze episode [23]. The value of b_550 is closely related to the particle size and hygroscopicity. Iziomon and Lohmann concluded that the lower value of b (0.11) during haze events is indicative of the aged character and particle growth of smoke aerosols [56]. As mentioned above, aerosols undergo an aging process during the time of solidification and condensation, hydrophilic aerosols increase during transportation, and the decreased value of α_s indicates an increasing trend in particle size, all of which contributed to the lower value (0.10) of b_550 during the haze in Wuhan. The up-scatter fraction β and asymmetry parameter can be calculated according to the Henyey-Greenstein phase function, as shown in the following formulas [57]:

$$\beta = 0.082 + 1.85b - 2.97b^2 \quad (4)$$

$$b = \frac{1-g^2}{2g}\left(\frac{1}{\sqrt{1+g^2}} - \frac{1}{1+g}\right) \quad (5)$$

Table 2. Aerosol optical properties obtained during the study.

Date	$PM_{2.5}$ ($\mu g \cdot m^{-3}$)	BC ($\mu g \cdot m^{-3}$)	$BC/PM_{2.5}$	σ_s_550	σ_{ab}_532	α_s	b_550	g_550	β_550	ω_0
6 June 2012	26.00 (16.50, 46.50)	2.71 (1.11, 4.67)	0.09 (0.04, 0.17)	0.22 (0.13, 0.35)	0.02 (0.01, 0.04)	1.60 (1.54, 1.85)	0.10 (0.09, 0.11)	0.66 (0.62, 0.68)	0.24 (0.23, 0.25)	0.92 (0.87, 0.96)
7 June 2012	35.00 (26.00, 54.50)	2.90 (2.33, 4.91)	0.07 (0.05, 0.17)	0.39 (0.29, 0.54)	0.02 (0.02, 0.04)	1.49 (1.17, 1.56)	0.09 (0.09, 0.10)	0.67 (0.65, 0.68)	0.23 (0.23, 0.24)	0.95 (0.89, 0.96)
8 June 2012	36.00 (22.50, 41.00)	2.65 (2.22, 3.20)	0.07 (0.06, 0.11)	0.27 (0.17, 0.36)	0.02 (0.02, 0.03)	1.57 (1.46, 1.71)	0.10 (0.09, 0.11)	0.66 (0.62, 0.68)	0.24 (0.23, 0.25)	0.93 (0.89, 0.95)
9 June 2012	29.00 (23.50, 36.0)	2.74 (2.33, 3.92)	0.10 (0.08, 0.13)	0.22 (0.13, 0.30)	0.02 (0.02, 0.03)	1.72 (1.57, 1.90)	0.11 (0.10, 0.12)	0.62 (0.61, 0.66)	0.25 (0.24, 0.26)	0.91 (0.87, 0.93)
10 June 2012	31.00 (25.00, 43.0)	2.91 (1.71, 4.34)	0.08 (0.06, 0.12)	0.23 (0.15, 0.41)	0.02 (0.01, 0.04)	1.72 (1.63, 1.79)	0.10 (0.10, 0.11)	0.65 (0.63, 0.67)	0.24 (0.23, 0.25)	0.92 (0.89, 0.94)
11 June 2012	304.00 (22.00, 553.50)	11.58 (2.22, 15.63)	0.03 (0.02, 0.13)	2.45 (0.21, 3.65)	0.10 (0.02, 0.13)	1.52 (1.39, 1.64)	0.10 (0.10, 0.10)	0.66 (0.66, 0.67)	0.23 (0.23, 0.24)	0.96 (0.92, 0.97)
12 June 2012	242.00 (115.50, 384.0)	8.34 (5.45, 10.23)	0.03 (0.02, 0.07)	1.28 (0.50, 2.05)	0.07 (0.05, 0.08)	1.66 (1.52, 1.80)	0.11 (0.10, 0.12)	0.64 (0.61, 0.67)	0.24 (0.23, 0.26)	0.95 (0.89, 0.97)
13 June 2012	130.00 (83.50, 168.50)	5.89 (2.85, 7.90)	0.05 (0.03, 0.06)	0.59 (0.29, 0.84)	0.05 (0.02, 0.07)	1.61 (1.50, 1.66)	0.11 (0.10, 0.12)	0.63 (0.60, 0.65)	0.24 (0.24, 0.26)	0.93 (0.89, 0.94)
14 June 2012	132.50 (108.50, 139.0)	5.70 (4.44, 6.89)	0.05 (0.04, 0.05)	0.54 (0.46, 0.75)	0.05 (0.04, 0.06)	1.46 (1.36, 1.53)	0.10 (0.10, 0.11)	0.65 (0.65, 0.67)	0.24 (0.23, 0.24)	0.93 (0.92, 0.95)

Median values are stated on the top line and the 10th and 90th percentiles are stated underneath within the parentheses.

Changes in β_550 and g_550 during the experimental period are shown in Figure 4c. It can be seen that the value of g_550 was higher (*i.e.*, remaining at ~0.65) during the haze days of 10–12 June. This shows that aerosol forward scattering played a dominant role during the haze. In the NCP, the value of g was found to be 0.66 due to the growth of aged particles, which is similar to our results [23].

The value of β_550 remained at ~0.23 from 10–12 June, which can be considered as a low level. With increasing concentration of aerosol particles, the total amount of scattered light would increase, as would light scattered back into space and backscattered light. However, the ratio of the light scattered back into space to the total scattered light (β_550) would not necessarily increase. The study by Zhang *et al.* showed that the up-scatter fraction was 0.24, which is similar to our findings. Lower β values mean that haze pollutants can heat the atmosphere more efficiently [23] and in our study, the low value of β (0.23) indicates a heating effect on the air, which is consistent with the increased atmospheric temperature mentioned above. The aerosol optical properties measured during the study are summarized in Table 2.

3.3.2. Aerosol Absorption Properties

The aerosol absorption coefficient σ_{ab} can reflect the absorption ability of aerosols. It can be measured directly through observing the amount of light attenuation using an aethalometer or calculated indirectly using BC concentration. Previous studies have described how to calculate σ_{ab} directly at any wavelength [58,59]; however, in this experiment, σ_{ab} was calculated indirectly based on the following formula:

$$\sigma_{ab} = \alpha \cdot [BC] \quad (6)$$

where α is the BC absorption efficiency conversion factor, which can be calculated according to the Mie theory or through linear regression between BC concentrations and aerosol absorption coefficients [60–62]. In this study, the value of α used was 8.28 $m^2 \cdot g^{-1}$. This was obtained through linear regression (with the correlation coefficient $R^2 = 0.92$) of the aerosol absorption coefficients (units: Mm^{-1}) measured by PAS at 532 nm and BC concentrations (units: $\mu g \cdot m^{-3}$) measured by the aethalometer at 880 nm [63]. Yan *et al.* used this value at the Shangdianzi (SDZ) Station [64] in northern China, and Zhao *et al.* also used this value in the NCP [3]. The value of 8.28 $m^2 \cdot g^{-1}$ is higher than the optimal estimated value provided by Bergin (8 $m^2 \cdot g^{-1}$) [65] and Bond (7.5 $m^2 \cdot g^{-1}$) [66], and lower than that obtained in Colorado (10 $m^2 \cdot g^{-1}$) [67] and the Mexico City Metropolitan Area (8–10 $m^2 \cdot g^{-1}$) [68]. Fuller *et al.* found that the α value is low (7 $m^2 \cdot g^{-1}$) for diesel soot [69]. Table 3 lists the BC absorption efficiency conversion factor α for the different sites.

Table 3. BC absorption efficiency conversion factor α at different sites.

Site	α($m^2 \cdot g^{-1}$)	Reference
Urban Guangzhou, southern China	8.28	[63]
BTH, China	8.28	[3]
Texas, USA	8.5	Big Bend Regional Aerosol and Visibility Observation Study (BRAVO) [61]
SDZ, China	8.28	[64]
Urban Beijing, China	8	[65]
Urban, Illinois, USA	7.5	[66]
Colorado, USA	10	Often used for urban aerosols [67]
Mexico City, Mexico	~8–10	[68]
Colorado, USA	7	Diesel soot [69]

Figure 4a shows the variability of σ_{ab}_532. It increased sharply during the haze period and reached a maximum value (0.15 km^{-1}) in the afternoon of 11 June. The mean values during the haze period and non-haze period were 0.086 and 0.025 km^{-1}, respectively, *i.e.*, the former was approximately 3.4 times the latter. The results of Zhao *et al.* reveal that the mean absorption coefficient during haze periods is 0.056 km^{-1} in the NCP, which is 5.2 times that during non-haze periods [3]. Additionally, the study by Ma *et al.* [49] at Wuqing indicates that the mean absorption coefficients during air pollution events in summer and spring were 0.11 and 0.09 km^{-1}, respectively. The mean value of σ_{ab}_532 in Wuhan was larger than that in the NCP and similar to that at Wuqing, which shows that summer haze pollution from transported biomass combustion is a serious problem in central China.

3.3.3. Single Scattering Albedo

The single scattering albedo (SSA) ω_0 is defined as the ratio of the scattering coefficient to the extinction coefficient of particles; the latter is the sum of the absorption and scattering coefficients. The value of ω_0 can reflect directly the aerosol radiative forcing and reveal the relationship between scattering and absorption coefficients [70]. For example, the value of ω_0 for a pure BC particle is only 0.2, which indicates that the BC particle has stronger light absorption ability than scattering ability. The value of ω_0 is related to the size and composition of the aerosols [23] and it can be obtained using integrated nephelometer and aethalometer. When calculating the SSA, the absorption and scattering coefficients should be corrected to the uniform wavelength. In the present study, the SSA was calculated at the wavelength of 532 nm. The details of the specific algorithm used can be found in a previous study [71].

As shown in Figure 4d, ω_0 increased rapidly to ~0.97 from the morning of 11 June and remained high throughout the haze days. During polluted conditions, the values of ω_0 were 0.89 at Wuqing [69] and ~0.86 in Beijing [72], both of which are lower than that found in Wuhan. This indicates that pollutants in Wuhan produced by biomass burning, rather than by local emissions, are more serious. Zhang *et al.* found that larger values of ω_0 are observed when RH is higher [23], *i.e.*, the water uptake by aerosol particles results in higher ω_0 [73], and the increasing trend in particle size produces non-light-absorbing components. In summary, the aged aerosols could generate coating effects, which increase light absorption. The solidification and condensation processes and secondary particles could increase light scattering, overcoming the increase of absorption resulting from increases of ω_0 [74]. The high values of ω_0 coincide with the decreases of α_s and b, both of which are related to the growth and aging characteristics of aerosols. Mie theory demonstrates that as aerosols grow in size and age by condensation during transport, their mass scattering efficiency increases, leading to an increase in ω_0 [55]. Overall, changes in the composition and size of the aerosols caused the higher values of ω_0 observed during the haze episode.

3.3.4. Aerosol Vertical Structure during Haze

Ground-based observations could provide information about surface aerosol properties through field experiments. However, the vertical distribution of particles is also needed in order to obtain detailed information on the spatial structure of pollutants during haze events. Seasonal variations in the vertical distribution of aerosols have been studied employing Raman Lidar at Shangdianzi station. It has been established that a two-layer structure exists in haze events [75]. The present study made use

of the CALIPSO 532 nm total attenuated backscatter coefficient $\beta'_{532,\mathrm{Total}}(z)$, volume depolarization ratio $V(z)$, total attenuated color ratio $X(z)$, and aerosol sub-layer classification product to explore the aerosol vertical structure. The variables can be calculated separately according to the following formulas (http://www-calipso.larc. nasa.gov/resources/calipso_users_guide/browse/index.php):

$$\beta'_{532,\mathrm{Total}}(z) = [\beta_{\parallel}(z) + \beta_{\perp}(z)]T^2_{532}(z) \tag{7}$$

Here, $\beta_{\parallel}(z)$ and $\beta_{\perp}(z)$ are the backscatter coefficients of the perpendicular channel and the parallel channel at height z for wavelength 532 nm, respectively, and $T^2_{532}(z)$ is the atmospheric bidirectional transmission at the wavelength of 532 nm. It is computed using the following formula:

$$T^2_{532}(z) = \exp\left\{-2\int_{z}^{z_{\mathrm{sat}}}\left[\sigma_{\mathrm{m}}(z') + \sigma_{\mathrm{a}}(z') + \sigma_{\mathrm{o_3}}(z')\right]dz'\right\} \tag{8}$$

where σ_{m}, σ_{a}, and $\sigma_{\mathrm{o_3}}$ are the extinction coefficients of atmospheric molecules, aerosols, and ozone, respectively, and z_{sat} represents the height of the satellite. The volume depolarization ratio $V(z)$ is defined as the ratio of the perpendicular channel to the parallel channel:

$$V(z) = \frac{\beta'_{532,\perp}(z)}{\beta'_{532,\parallel}(z)} \tag{9}$$

$V(z)$ can reflect the irregularity and non-spherical features of the particles. The total attenuated color ratio $X(z)$ is defined as the ratio of backscattering energy at 1064 nm to that at 532 nm, which can reflect particle size; the larger the size, the larger the value of $X(z)$. It can be defined as follows:

$$X(z) = \frac{\beta'_{1064}(z)}{\beta'_{532,\mathrm{Total}}(z)} \tag{10}$$

As shown in Figure 1b, the CALIPSO satellite passed over Wuhan (29.00°–32.00°N, 113.91°E) at 02:19:48 (LZT) on 12 June 2012, which was the day with the most severe haze. Figure 5a shows the total attenuated backscatter coefficient for the 532-nm orbit height section of CALIPSO over Wuhan. For most cases, the green–yellow–orange colors represent the characteristics of the aerosols, whereas the red–gray–white colors represent the characteristics of the optically thick aerosol layer or optically thin clouds. Blue usually represents areas without signals [42]. Aerosols can be seen primarily at altitudes lower than 3 km, and their concentrations decrease considerably with height. The major components of the atmosphere above 5 km are air molecules. The CALIPSO Level 2 aerosol sub-layer classification product can be used to identify the types of aerosols (e.g., clean marine aerosols, dust aerosols, polluted continental aerosols, clean continental aerosols, polluted dust aerosols, and smoke aerosols).

As shown in Figure 5b, several prominent stratifications can be seen below 3 km. During the haze episode, there were two main segments: a polluted dust aerosol layer and a polluted continental aerosol layer. It can be seen in Figure 5c that most values of $V(z)$ are below 0.2 between heights of 0–6 km, which indicates that the aerosols were primarily regular shapes. Figure 5d shows that $X(z)$ is mainly 0.5–1.0 within the height range of 0–1.5 km, which indicates that particle sizes are not large at low altitudes, which is consistent with the α_s values obtained from the ground-based nephelometer.

Figure 6 shows the mean extinction coefficient profiles from the CALIPSO Level 2 aerosol profile product. The blue and red colors represent the profiles not processed and processed by quality

screening, respectively. Below 1 km height, the extinction coefficient remains as high as 1 km^{-1}, which was very close to the mean extinction coefficient (1.27 km^{-1}) measured by the nephelometer and aethalometer on the ground surface. The extinction coefficient then gradually decreases above 1 km, which indicates that the highest concentration of pollutants was below 1 km.

Figure 5. Information on structure of aerosol vertical distribution from CALIPSO at 02:19:48 (LZT) on 12 June 2012. (**a**) 532 nm total attenuated backscatter coefficient; (**b**) Level 2 aerosol sub-layer classification information ("−1": undefined signal, "0": clean marine aerosol, "1": dust aerosol, "2": polluted continent aerosol, "3": clean continent aerosol, "4": polluted dust aerosol, and "5": smoke aerosol); (**c**) Volume depolarization ratio; (**d**) Total attenuated color ratio.

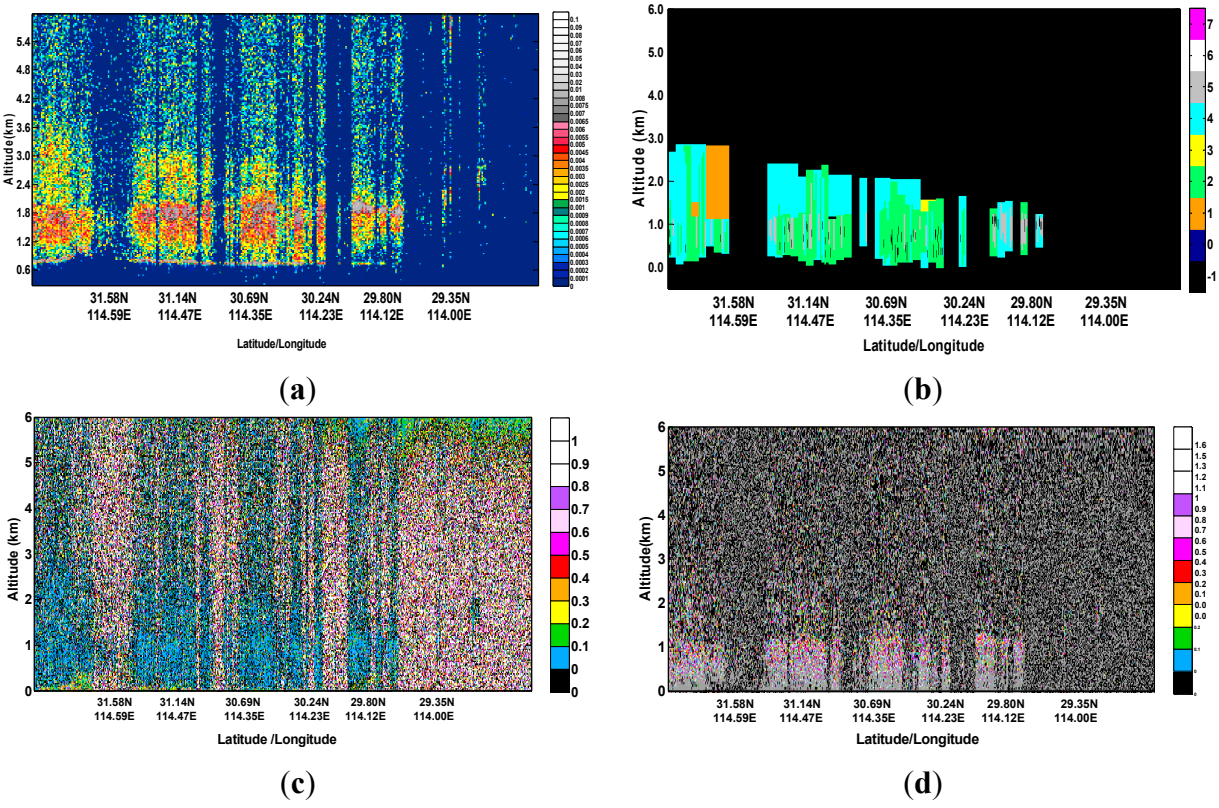

Figure 6. Information on aerosol extinction coefficient profile from CALIPSO at 02:19:48 (LZT) on 12 June 2012 (blue: without quality screening; red: with quality screening).

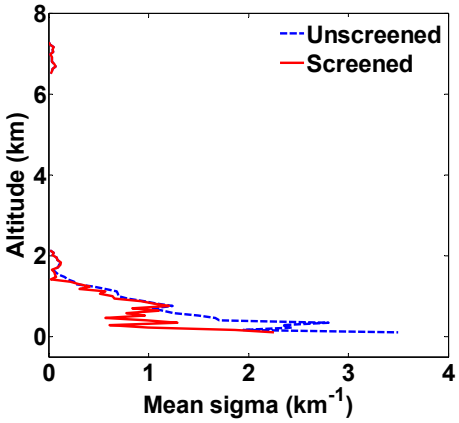

4. Conclusions

A severe haze episode that occurred in central China (Wuhan) from 6–14 June 2012 was studied. The aerosol optical properties during the haze event were measured using ground-based equipment (nephelometer, aethalometer, meteorological station, and particle detector) and satellite (CALIPSO). The haze was caused mostly by the long-distance transport of particles from the combustion of biomass (such as straw) during the harvest season in northern Anhui Province. During the haze days, the mean mass concentrations of $PM_{2.5}$ and BC were 9.9 (332.79 *versus* 33.66 $\mu g \cdot m^{-3}$) and 3.2 times (9.67 *versus* 2.99 $\mu g \cdot m^{-3}$) greater, respectively, than during normal weather. The large aerosol loading contributed to the high coefficients of aerosol scattering coefficient (2.32 km^{-1}) and absorption (0.086 km^{-1}). Particle size became larger consistent with the reduced scattering Ångström exponents. The high asymmetry parameter (0.65) and SSA (~0.97) observed during the haze coincided with the relatively low backscatter ratio (0.11) and up-scatter fraction (0.23), which were related to the increased particle size and led to a heating effect on the atmosphere. Pollutants accumulated primarily below the height of 3 km and their shapes remained regular. The mean extinction coefficient (~1 km^{-1}) derived from CALIPSO was very close to that (1.27 km^{-1}) obtained by the ground-based equipment, which revealed good agreement between the two types of observations.

Acknowledgments

This study was supported financially by the Haze Program of the Wuhan Technological Bureau, National Basic Research Program (Grant No. 2011CB707106), and the National Natural Science Foundation of China (NSFC) (Program No. 41127901). We would like to thank the NASA Langley Research Center for providing the CALIPSO data. We also thank the editor for help with refining the manuscript.

Author Contributions

The study was completed with cooperation between all authors. Miao Zhang and Wei Gong designed the research topic. Miao Zhang conducted the experiment and wrote the paper. Yingying Ma and Zhongmin Zhu checked the experimental result. All authors agreed to the manuscript being submitted.

Conflicts of Interest

The authors declare no conflicts of interest.

References

1. Solomon, S. *Climate Change 2007—The Physical Science Basis: Working Group in Contribution to the Fourth Assessment Report of the IPCC*; Cambridge University Press: Cambridge, UK, 2007; Volume 4.
2. Ackerman, A.S.; Toon, O.; Stevens, D.; Heymsfield, A.; Ramanathan, V.; Welton, E. Reduction of tropical cloudiness by soot. *Science* **2000**, *288*, 1042–1047.

3. Zhao, X.; Zhao, P.; Xu, J.; Meng, W.; Pu, W.; Dong, F.; He, D.; Shi, Q. Analysis of a winter regional haze event and its formation mechanism in the north china plain. *Atmos. Chem. Phys.* **2013**, *13*, 5685–5696.
4. World Health Organization. *Health Aspects of Air Pollution: Results from the WHO Project* S*ystematic Review of Health Aspects of Air Pollution in Europe*; World Health Organization, Regional Office for Europe: Copenhagen, Denmark, 2004.
5. Parrish, D.D.; Zhu, T. Clean air for megacities. *Science* **2009**, *326*, 674–675.
6. Zhao, P.; Zhang, X.; Xu, X.; Zhao, X. Long-term visibility trends and characteristics in the region of Beijing, Tianjin, and Hebei, China. *Atmos. Res.* **2011**, *101*, 711–718.
7. Lee, K.H.; Kim, Y.J.; Kim, M.J. Characteristics of aerosols observed during two severe haze events over Korea in June and October 2004. *Atmos. Environ.* **2006**, *40*, 5146–5155.
8. Li, Z.; Xia, X.; Cribb, M.; Mi, W.; Holben, B.; Wang, P.; Chen, H.; Tsay, S.C.; Eck, T.; Zhao, F. Aerosol optical properties and their radiative effects in northern China. *J. Geophys. Res.: Atmos.* **2007**, doi:10.1029/2006JD007382.
9. See, S.; Balasubramanian, R.; Wang, W. A study of the physical, chemical, and optical properties of ambient aerosol particles in Southeast Asia during hazy and non-hazy days. *J. Geophys. Res.: Atmos.* **2006**, doi:10.1029/2005JD006180.
10. Sun, Y.; Zhuang, G.; Tang, A.; Wang, Y.; An, Z. Chemical characteristics of $PM_{2.5}$ and PM_{10} in haze-fog episodes in Beijing. *Environ. Sci. Technol.* **2006**, *40*, 3148–3155.
11. Tan, J.-H.; Duan, J.-C.; Chen, D.-H.; Wang, X.-H.; Guo, S.-J.; Bi, X.-H.; Sheng, G.-Y.; He, K.-B.; Fu, J.-M. Chemical characteristics of haze during summer and winter in Guangzhou. *Atmos. Res.* **2009**, *94*, 238–245.
12. Kang, H.; Zhu, B.; Su, J.; Wang, H.; Zhang, Q.; Wang, F. Analysis of a long-lasting haze episode in Nanjing, China. *Atmos. Res.* **2013**, *120*, 78–87.
13. Lau, K.M.; Kim, K.M. Observational relationships between aerosol and Asian monsoon rainfall, and circulation. *Geophys. Res. Lett.* **2006**, doi:10.1029/2006GL027546.
14. Lau, K.M.; Kim, M.K.; Kim, K.M. Asian summer monsoon anomalies induced by aerosol direct forcing: The role of the Tibetan Plateau. *Clim. Dyn.* **2006**, *26*, 855–864.
15. Lau, K.-M.; Ramanathan, V.; Wu, G.-X.; Li, Z.; Tsay, S.; Hsu, C.; Sikka, R.; Holben, B.; Lu, D.; Tartari, G. The joint aerosol-monsoon experiment. *Bull. Am. Meteorol. Soc.* **2008**, *89*, 369–383.
16. Wang, Y.; Che, H.; Ma, J.; Wang, Q.; Shi, G.; Chen, H.; Goloub, P.; Hao, X. Aerosol radiative forcing under clear, hazy, foggy, and dusty weather conditions over Beijing, China. *Geophys. Res. Lett.* **2009**, doi:10.1029/2009GL037181.
17. Ramanathan, V.; Crutzen, P.J.; Lelieveld, J.; Mitra, A.; Althausen, D.; Anderson, J.; Andreae, M.; Cantrell, W.; Cass, G.; Chung, C. Indian ocean experiment: An integrated analysis of the climate forcing and effects of the great Indo—Asian haze. *J. Geophys. Res.: Atmos.* **2001**, *106*, 28371–28398.
18. Xia, X.; Chen, H.; Wang, P.; Zhang, W.; Goloub, P.; Chatenet, B.; Eck, T.; Holben, B. Variation of column-integrated aerosol properties in a Chinese urban region. *J. Geophys. Res.: Atmos.* **2006**, doi:10.1029/2005JD006203.
19. Ramanathan, V.; Carmichael, G. Global and regional climate changes due to black carbon. *Nat. Geosci.* **2008**, *1*, 221–227.

20. Pósfai, M.; Buseck, P.R. Nature and climate effects of individual tropospheric aerosol particles. **2010**, *38*, 17–43.
21. Chameides, W.L.; Yu, H.; Liu, S.; Bergin, M.; Zhou, X.; Mearns, L.; Wang, G.; Kiang, C.; Saylor, R.; Luo, C. Case study of the effects of atmospheric aerosols and regional haze on agriculture: An opportunity to enhance crop yields in China through emission controls? *Proc. Natl. Acad. Sci.* **1999**, *96*, 13626–13633.
22. Li, W.; Zhou, S.; Wang, X.; Xu, Z.; Yuan, C.; Yu, Y.; Zhang, Q.; Wang, W. Integrated evaluation of aerosols from regional brown hazes over northern China in winter: Concentrations, sources, transformation, and mixing states. *J. Geophys. Res.: Atmos.* **2011**, doi:10.1029/2010JD015099.
23. Zhang, X.; Huang, Y.; Zhu, W.; Rao, R. Aerosol characteristics during summer haze episodes from different source regions over the coast city of North China Plain. *J. Quant. Spectrosc. Radiat. Transf.* **2013**, *122*, 180–193.
24. Chakrabarty, R.K.; Garro, M.A.; Wilcox, E.M.; Moosmüller, H. Strong radiative heating due to wintertime black carbon aerosols in the Brahmaputra River valley. *Geophys. Res. Lett.* **2012**, doi:10.1029/2012GL051148.
25. Thornhill, K.L.; Chen, G.; Dibb, J.; Jordan, C.E.; Omar, A.; Winstead, E.L.; Schuster, G.; Clarke, A.; McNaughton, C.; Scheuer, E. The impact of local sources and long-range transport on aerosol properties over the northeast U.S. region during INTEX-NA. *J. Geophys. Res.: Atmos.* **2008**, doi:10.1029/2007JD008666.
26. Li, W.; Shao, L.; Buseck, P. Haze types in Beijing and the influence of agricultural biomass burning. *Atmos. Chem. Phys.* **2010**, *10*, 8119–8130.
27. Duan, F.; Liu, X.; Yu, T.; Cachier, H. Identification and estimate of biomass burning contribution to the urban aerosol organic carbon concentrations in Beijing. *Atmos. Environ.* **2004**, *38*, 1275–1282.
28. Anderson, T.; Covert, D.; Marshall, S.; Laucks, M.; Charlson, R.; Waggoner, A.; Ogren, J.; Caldow, R.; Holm, R.; Quant, F. Performance characteristics of a high-sensitivity, three-wavelength, total scatter/backscatter nephelometer. *J. Atmos. Ocean. Technol.* **1996**, *13*, 967–986.
29. Heintzenberg, J.; Charlson, R.J. Design and applications of the integrating nephelometer: A review. *J. Atmos. Ocean. Technol.* **1996**, *13*, 987–1000.
30. Anderson, T.L.; Ogren, J.A. Determining aerosol radiative properties using the TSI 3563 integrating nephelometer. *Aerosol Sci. Technol.* **1998**, *29*, 57–69.
31. Lyamani, H.; Olmo, F.; Alados-Arboledas, L. Light scattering and absorption properties of aerosol particles in the urban environment of Granada, Spain. *Atmos. Environ.* **2008**, *42*, 2630–2642.
32. Wang, L.; Gong, W.; Li, C.; Lin, A.; Hu, B.; Ma, Y. Measurement and estimation of photosynthetically active radiation from 1961 to 2011 in central China. *Appl. Energy* **2013**, *111*, 1010–1017.
33. Kaufman, Y.J.; Justice, C.O.; Flynn, L.P.; Kendall, J.D.; Prins, E.M.; Giglio, L.; Ward, D.E.; Menzel, W.P.; Setzer, A.W. Potential global fire monitoring from EOS-MODIS. *J. Geophys. Res.: Atmos.* **1998**, *103*, 32215–32238.
34. Justice, C.; Giglio, L.; Korontzi, S.; Owens, J.; Morisette, J.; Roy, D.; Descloitres, J.; Alleaume, S.; Petitcolin, F.; Kaufman, Y. The MODIS fire products. *Remote Sens. Environ.* **2002**, *83*, 244–262.
35. Giglio, L.; Descloitres, J.; Justice, C.O.; Kaufman, Y.J. An enhanced contextual fire detection algorithm for MODIS. *Remote Sens. Environ.* **2003**, *87*, 273–282.

36. Morisette, J.T.; Giglio, L.; Csiszar, I.; Justice, C.O. Validation of the MODIS active fire product over southern Africa with ASTER data. *Int. J. Remote Sens.* **2005**, *26*, 4239–4264.
37. Csiszar, I.A.; Morisette, J.T.; Giglio, L. Validation of active fire detection from moderate-resolution satellite sensors: The MODIS example in northern Eurasia. *IEEE Trans. Geosci. Remote Sens.* **2006**, *44*, 1757–1764.
38. Giglio, L. *MODIS Collection 5 Active Fire Product User's Guide Version 2.4*; Science Systems and Applications, Inc.: Maryland, MD, USA, 2010.
39. Winker, D.M.; Pelon, J.R.; McCormick, M.P. The CALIPSO mission: Spaceborne lidar for observation of aerosols and clouds. In *Third International Asia-Pacific Environmental Remote Sensing Remote Sensing of the Atmosphere, Ocean, Environment, and Space*; International Society for Optics and Photonics: Bellingham, WA, USA, 2003; pp. 1–11.
40. Winker, D.; Pelon, J.; McCormick, M. Initial results from CALIPSO. In Proceedings of the 23rd International Laser Radar Conference, Nara, Japan, 24–28 July 2006; pp. 991–994.
41. Winker, D.M.; Hunt, W.H.; McGill, M.J. Initial performance assessment of CALIOP. *Geophys. Res. Lett.* **2007**, doi:10.1029/2007GL030135.
42. Liu, Z.; Liu, D.; Huang, J.; Vaughan, M.; Uno, I.; Sugimoto, N.; Kittaka, C.; Trepte, C.; Wang, Z.; Hostetler, C. Airborne dust distributions over the Tibetan Plateau and surrounding areas derived from the first year of CALIPSO lidar observations. *Atmos. Chem. Phys.* **2008**, *8*, 5045–5060.
43. Tao, M.; Chen, L.; Su, L.; Tao, J. Satellite observation of regional haze pollution over the North China Plain. *J. Geophys. Res.: Atmos.* **2012**, doi:10.1029/2012JD017915.
44. Huang, J.; Minnis, P.; Yi, Y.; Tang, Q.; Wang, X.; Hu, Y.; Liu, Z.; Ayers, K.; Trepte, C.; Winker, D. Summer dust aerosols detected from CALIPSO over the Tibetan Plateau. *Geophys. Res. Lett.* **2007**, doi:10.1029/2007GL029938.
45. Chen, Y.; Liu, Q.; Geng, F.; Zhang, H.; Cai, C.; Xu, T.; Ma, X.; Li, H. Vertical distribution of optical and micro-physical properties of ambient aerosols during dry haze periods in Shanghai. *Atmos. Environ.* **2012**, *50*, 50–59.
46. Vautard, R.; Yiou, P.; van Oldenborgh, G.J. Decline of fog, mist and haze in Europe over the past 30 years. *Nat. Geosci.* **2009**, *2*, 115–119.
47. Quan, J.; Zhang, Q.; He, H.; Liu, J.; Huang, M.; Jin, H. Analysis of the formation of fog and haze in North China Plain (NCP). *Atmos. Chem. Phys.* **2011**, *11*, 8205–8214.
48. Deng, X.; Shi, C.; Wu, B.; Chen, Z.; Nie, S.; He, D.; Zhang, H. Analysis of aerosol characteristics and their relationships with meteorological parameters over Anhui Province in China. *Atmos. Res.* **2012**, *109*, 52–63.
49. Ma, N.; Zhao, C.; Nowak, A.; Müller, T.; Pfeifer, S.; Cheng, Y.; Deng, Z.; Liu, P.; Xu, W.; Ran, L. Aerosol optical properties in the North China Plain during HaChi campaign: An *in-situ* optical closure study. *Atmos. Chem. Phys.* **2011**, *11*, 5959–5973.
50. Balis, D.; Amiridis, V.; Zerefos, C.; Gerasopoulos, E.; Andreae, M.; Zanis, P.; Kazantzidis, A.; Kazadzis, S.; Papayannis, A. Raman lidar and sunphotometric measurements of aerosol optical properties over Thessaloniki, Greece during a biomass burning episode. *Atmos. Environ.* **2003**, *37*, 4529–4538.

51. Huang, X.-F.; Yu, J.Z. Size distributions of elemental carbon in the atmosphere of a coastal urban area in South China: Characteristics, evolution processes, and implications for the mixing state. *Atmos. Chem. Phys.* **2008**, *8*, 5843–5853.
52. Eck, T.; Holben, B.; Reid, J.; Dubovik, O.; Smirnov, A.; O'neill, N.; Slutsker, I.; Kinne, S. Wavelength dependence of the optical depth of biomass burning, urban, and desert dust aerosols. *J. Geophys. Res.: Atmos.* **1999**, *104*, 31333–31349.
53. Eck, T.; Holben, B.; Ward, D.; Dubovik, O.; Reid, J.; Smirnov, A.; Mukelabai, M.; Hsu, N.; O'neill, N.; Slutsker, I. Characterization of the optical properties of biomass burning aerosols in Zambia during the 1997 ZIBBEE field campaign. *J. Geophys. Res.: Atmos.* **2001**, *106*, 3425–3448.
54. O'Neill, N.; Eck, T.; Holben, B.; Smirnov, A.; Royer, A.; Li, Z. Optical properties of boreal forest fire smoke derived from sun photometry. *J. Geophys. Res.: Atmos.* **2002**, doi:10.1029/2001JD000877.
55. Abdalmogith, S.S.; Harrison, R.M.; Derwent, R.G. Particle sulphate and nitrate in southern England and Northern Ireland during 2002/3 and its formation in a photochemical trajectory model. *Sci. Total Environ.* **2006**, *368*, 769–780.
56. Iziomon, M.G.; Lohmann, U. Optical and meteorological properties of smoke-dominated haze at the ARM Southern Great Plains Central Facility. *Geophys. Res. Lett.* **2003**, doi:10.1029/2002GL016606.
57. Chakrabarty, R.; Moosmüller, H.; Chen, L.-W.; Lewis, K.; Arnott, W.; Mazzoleni, C.; Dubey, M.; Wold, C.; Hao, W.; Kreidenweis, S. Brown carbon in tar balls from smoldering biomass combustion. *Atmos. Chem. Phys.* **2010**, *10*, 6363–6370.
58. Bodhaine, B.A. Aerosol absorption measurements at Barrow, Mauna Loa and the South Pole. *J. Geophys. Res.: Atmos.* **1995**, *100*, 8967–8975.
59. Weingartner, E.; Saathoff, H.; Schnaiter, M.; Streit, N.; Bitnar, B.; Baltensperger, U. Absorption of light by soot particles: Determination of the absorption coefficient by means of aethalometers. *J. Aerosol Sci.* **2003**, *34*, 1445–1463.
60. Arnott, W.; Moosmüller, H.; Sheridan, P.; Ogren, J.; Raspet, R.; Slaton, W.; Hand, J.; Kreidenweis, S.; Collett, J. Photoacoustic and filter-based ambient aerosol light absorption measurements: Instrument comparisons and the role of relative humidity. *J. Geophys. Res.: Atmos.* **2003**, doi:10.1029/2002JD002165.
61. Arnott, W.P.; Hamasha, K.; Moosmüller, H.; Sheridan, P.J.; Ogren, J.A. Towards aerosol light-absorption measurements with a 7-wavelength aethalometer: Evaluation with a photoacoustic instrument and 3-wavelength nephelometer. *Aerosol Sci. Technol.* **2005**, *39*, 17–29.
62. Clarke, A.D.; Charlson, R.J. Radiative properties of the background aerosol: Absorption component of extinction. *Science* **1985**, *229*, 263–265.
63. Schmid, O.; Chand, D.; Andreae, M.O. Aerosol optical properties in urban Guangzhou. In Proceedings of PRD Workshop, Beijing, China, 13–14 January 2005.
64. Yan, P.; Tang, J.; Huang, J.; Mao, J.; Zhou, X.; Liu, Q.; Wang, Z.; Zhou, H. The measurement of aerosol optical properties at a rural site in northern China. *Atmos. Chem. Phys.* **2008**, *8*, 2229–2242.
65. Bergin, M.; Cass, G.; Xu, J.; Fang, C.; Zeng, L.; Yu, T.; Salmon, L.; Kiang, C.; Tang, X.; Zhang, Y. Aerosol radiative, physical, and chemical properties in Beijing during June 1999. *J. Geophys. Res.: Atmos.* **2001**, *106*, 17969–17980.
66. Bond, T.C.; Bergstrom, R.W. Light absorption by carbonaceous particles: An investigative review. *Aerosol Sci. Technol.* **2006**, *40*, 27–67.

67. Moosmüller, H.; Arnott, W.; Rogers, C.; Chow, J.; Frazier, C.; Sherman, L.; Dietrich, D. Photoacoustic and filter measurements related to aerosol light absorption during the northern front range air quality study (Colorado 1996/1997). *J. Geophys. Res.: Atmos.* **1998**, *103*, 28149–28157.
68. Barnard, J.; Kassianov, E.; Ackerman, T.; Frey, S.; Johnson, K.; Zuberi, B.; Molina, L.; Molina, M.; Gaffney, J.; Marley, N. Measurements of black carbon specific absorption in the Mexico City metropolitan area during the MCMA 2003 field campaign. *Atmos. Chem. Phys. Discuss.* **2005**, *5*, 4083–4113.
69. Fuller, K.A.; Malm, W.C.; Kreidenweis, S.M. Effects of mixing on extinction by carbonaceous particles. *J. Geophys. Res.: Atmos.* **1999**, *104*, 15941–15954.
70. Takemura, T.; Nakajima, T.; Dubovik, O.; Holben, B.N.; Kinne, S. Single-scattering albedo and radiative forcing of various aerosol species with a global three-dimensional model. *J. Clim.* **2002**, *15*, 333–352.
71. Virkkula, A.; Ahlquist, N.C.; Covert, D.S.; Arnott, W.P.; Sheridan, P.J.; Quinn, P.K.; Coffman, D.J. Modification, calibration and a field test of an instrument for measuring light absorption by particles. *Aerosol Sci. Technol.* **2005**, *39*, 68–83.
72. Jung, J.; Lee, H.; Kim, Y.J.; Liu, X.; Zhang, Y.; Hu, M.; Sugimoto, N. Optical properties of atmospheric aerosols obtained by *in situ* and remote measurements during 2006 campaign of air quality research in Beijing (CAREBeijing-2006). *J. Geophys. Res.: Atmos.* **2009**, doi:10.1029/2008JD010337.
73. Cheng, Y.F.; Wiedensohler, A.; Eichler, H.; Heintzenberg, J.; Tesche, M.; Ansmann, A.; Wendisch, M.; Su, H.; Althausen, D.; Herrmann, H.; *et al.* Relative humidity dependence of aerosol optical properties and direct radiative forcing in the surface boundary layer at Xinken in Pearl River Delta of China: An observation based numerical study. *Atmos. Environ.* **2008**, *42*, 6373–6397.
74. Cheng, Y.F.; Berghof, M.; Garland, R.M.; Wiedensohler, A.; Wehner, B.; Müller, T.; Su, H.; Zhang, Y.H.; Achtert, P.; Nowak, A.; *et al.* Influence of soot mixing state on aerosol light absorption and single scattering albedo during air mass aging at a polluted regional site in northeastern China. *J. Geophys. Res.: Atmos.* **2009**, doi:10.1029/2008JD010883.
75. Hänel, A.; Baars, H.; Althausen, D.; Ansmann, A.; Engelmann, R.; Sun, J.Y. One-year aerosol profiling with EUCAARI Raman lidar at Shangdianzi GAW station: Beijing plume and seasonal variations. *J. Geophys. Res.: Atmos.* **2012**, doi:10.1029/2012JD017577.